

Feasibility Study of Cold Gas Thrusters for GOMSPACE Cube-Sat

Compressible Flow Simulations in COMSOL Multiphysics

Joel Bjervig
Nils Gumaelius

Project in Computational Science: Report

August 24, 2022

UU_sigill_NV_gra.png

Contents

1	Sammanfattning	3
2	Introduction	4
3	Theory	6
3.1	A Brief Introduction to the Navier Stokes Equations	6
3.2	Non-isothermal Flow	6
3.3	Supersonic Flow	6
3.4	Compressible Flow	7
3.5	One-Dimensional Isentropic Pipe Flow	7
3.6	Thrust Efficiency and Shocks	12
3.7	Sutherlands Law	12
4	Numerical Methods and Solvers	14
4.1	GMRES	14
4.2	The Multigrid Method	17
5	Simulation Setup	19
5.1	COMSOL Multiphysics	19
5.2	Thruster Model	19
5.3	Exhaust Plume Model	22
5.4	Materials	22
5.5	Boundary Conditions	24
6	Results	24
6.1	Thruster Simulation	26
6.2	Exhaust Plume Simulation	28
7	Discussion	28
7.1	Meshing Options	28
7.2	Exhaust Plume Model Results	31
7.3	Fidelity of COMSOLs Solution	32
8	Conclusions	33

Abstract

In this project we perform a feasibility study of a cold gas thruster by simulating compressible flow of butane gas in COMSOL Multiphysics. The thruster is a thin chip, comprised of an inlet, a high-pressure chamber, followed by a converging-diverging nozzle through which the butane gas will reach supersonic speeds. The aim is to investigate how the thermal gradient of the thruster affects the velocity, pressure, temperature, and density of the gas. The temperature for maximum efficiency before the throat is given and to reach that target a heating element is placed in contact with the thruster. While most nozzles are axi-symmetric, this thruster has a rectangular cross-section. It is thus relevant to investigate the behavior of the exhaust plume for this distinct thruster shape. The subsequent exhaust plume might have instabilities in the form of shock waves, which decreases the efficiency of the thruster. COMSOL Multiphysics has a broad range of physics modules and numerical methods which can solve the approximated equations that the finite element method constructs. The study shows that the emissivity of the thruster chip has a large impact on the thermal gradient of the rocket and the gas. This is because the setup in COMSOL does not define any contact with the surrounding components of the propulsion device which in reality acts as heat sinks. The exhaust plume has an under-expanded flow, meaning maximal efficiency is not reached.

1 Sammanfattning

För att undersöka hur en kall-gas raketmotor presterar, simulerar vi i detta projekt ett kompressibelt flöde utav butangas i COMSOL Multiphysics. Raketen är tillverkat utav ett kisel chip som består av ett gas inlopp, en kammare för högtrycksgas och slutligen ett så kallat "converging diverging" munstycke där gasen flödar igenom för att nå supersoniska hastigheter. Målet med denna studie är att utreda hur den termiska gradienten av raketmotorn påverkar gasens hastighet, tryck, temperatur och densitet. Den föredragna temperaturen given av GomSpace är nådd strax innan munstycketets början genom ett litet värmeelement på utsidan av raketchipet. Medan de flesta raketmunstyckena är symmetriska längs en axel, har denna raketmotorn en rektangulär tvärsnittsarea. Raketers avgaspolymer kan ha instabiliteter i form av chockvågor, vilket minskar verkningsgraden på raketen. Därför är det av intresse att även undersöka avgaspolymer som initialt har en rektangulär tvärsnittsarea. COMSOL Multiphysics® är en kommersiellt tillgänglig mjukvara som kan lösa komplexa problem genom finita element och ett stort urval av avancerade numeriska metoder. Studien visar att raketens emissivitet har en avgörande roll i hur temperaturen fördelar sig i raketchipet och i gasen. I COMSOLs model är däremot raketen inte i fysisk kontakt med några andra komponenter som i verkligheten leder bort värme. Flödet av avgas visar sig vara asymmetrisk med tydliga diskontinuiteter längs med polymeren. Dessutom är gasen underexpanderat vilket pekar på att maximal effektivitet inte nås.

2 Introduction

Background

In the late 1950s a handful of satellites were sent up to low earth orbit, marking the start of the space age. Since then, 10-50 satellites has been placed in orbit annually until the 2010s when the number of satellites sent up skyrocketed, with roughly 1400 satellites in 2021. Behind this rapid growth lies the increased interest among large private companies and governments for satellites communication and remote sensing. With growing competition and continuing advancements in the industry, launch frequency continues to increase, and launch cost to decrease. A standard measure of the cost-effectiveness for a rocket is the payload cost; price per unit of cargo mass. This economic incentive has lead to the development of a standardized satellite system of nano-satelites, namely cubesats. They are smaller, lighter and much cheaper to send into space than traditional satellites, and roughly costs up to a million dollar ([1]). For comparison the traditional sized satellites are roughly the size of a bus and may cost billions of dollars ([1]). A standardized CubeSat unit has a cubic shape of side length 10 centimeter and weight about 1.3 kg. While the final size of the satellite varies the most common setup is a 2x3 CubeSat, containing six of these cubic modules. The standardization allows companies not only to mount units together to create larger satellites, but also enables collaborations between component manufactures to jointly create satellite products. This has revolutionized the satellite industry and makes sending up a satellite a possibility only a few global superpowers had before. The small size of the satellites limits the choice of propulsion systems. Classical thrusters that uses combustion are not possible to use due to their size and the high temperatures the chemical reactions creates. Instead, different simpler and smaller sized systems are commonly used. GomSpace is a Danish nano-satellite manufacturer based in Aarhus, Denmark, with its propulsion department situated in Uppsala, Sweden. One solution that GomSpace are working with are cold gas thrusters. These cold gas thursters uses no combustional propellant, but instead relies on high pressure butane gas. The nozzle has a geometry such that the gas reaches super sonic speeds to generate thrust. The GomSpace Nanoprop 6DOF propulsion component in Figure 1 has six micro-electro-mechanical systems (MEMS) thrusters, four at each corner and two along the sides, giving the propulsion module six degrees of freedom. The MEMS thrusters are roughly 2x1 cm and $350\mu\text{m}$ thin. Normally two of these propulsion modules are situated on opposite sides of a satellite.

Objective

The extreme environment of space sets high demands on the materials. Because testing is usually expensive, numerical simulations are essential in the development of thrusters. In this study the GomSpace cold gas thruster is modeled and studied in COMSOL Multiphysics. The study has three main goals:

1. Model a cold gas thruster in COMSOL to understand the heat transfer between the solid and the gas.



Figure 1: *The GomSpace Nanoprop 6DOF propulsion device. The MEMS thrusters are the small chips that can be seen in each corner and two along the sides.*

2. Investigate how different materials perform as the solid.
3. Examine the characteristics and dimension of the exhaust plume.

To reach these objectives a high mach number flow (hmnf) COMSOL model is created. The study of the model needs to contain both a fluid simulation of the gas, as well as a heat transfer simulation between the fluid, solid and space. Afterwards the solution is validated using the theory of compressible flow. Measured data of the fluids temperature, density, velocity and pressure at select areas of the thruster is given by GomSpace to compare the simulation with. Finally the temperature profile is analyzed using three different materials for the thruster chip. The exhaust plume is analyzed using a modified model.

Secrecy

The geometric parameters for the GomSpace thrusters are classified. Thus, to not limit the project, a similar "reference model", with the same characteristics is used.

3 Theory

3.1 A Brief Introduction to the Navier Stokes Equations

The Navier-Stokes equations are a system of nonlinear partial differential equations that describe the flow of a fluid and are written as follows

$$\frac{\partial \mathbf{u}}{\partial t} + \mathbf{u} \cdot \nabla \mathbf{u} = -\frac{\nabla}{\rho} \cdot \boldsymbol{\sigma} + \mathbf{F} \quad (1)$$

$$\boldsymbol{\sigma} = \frac{1}{\rho} \nabla \cdot (-p\mathbf{I} + \mathbf{K}). \quad (2)$$

They can be derived from the Cauchy momentum equation by expressing the Cauchy stress tensor $\boldsymbol{\sigma}$ as a sum of a pressure (volumetric stress) $p\mathbf{I}$ term and a viscous (deviatoric stress) term \mathbf{K} . Together with a wide range of discretization methods, numerical solvers and optimization methods the theory of fluid dynamics forms the basis for computational fluid dynamics ef.[2].

3.2 Non-isothermal Flow

Isothermal flow refers to the case when a fluid flow has negligible changes in temperature and is therefore assumed to be homogeneous in the simulations. This assumption is useful when modeling fluids that are not exposed to any heat sources or pressure changes that significantly alters the fluids temperature. Instead, a non-isothermal flow has a variable temperature through space and time. This case is of special interest when working with compressible flow, which introduces non-trivial changes in pressure and subsequently all other variables of the fluid ef.[2].

3.3 Supersonic Flow

The speed-region of transsonic and supersonic flow builds on the Mach number $M \equiv \frac{u}{c}$ and are used to assess the importance of the fluids compressibility. Consider an infinitesimal point submerged in a compressible fluid. The point source emits low pressure disturbances (acoustic waves) at the speed of sound c . In Figure 2, time is incremented by integers of Δt . In Figure 2 a), when the point source is stationary $u = 0$, the acoustic waves originates from the same location throughout time and are separated by a distance $c\Delta t$. In Figure 2 b) the point source starts moving at a subsonic speed $M < 1$. The propagating waves fronts now has different points of origin through time, separated by a distance $u\Delta t$. Thus the separating distance upstream between the wave fronts are now $(c-u)\Delta t$, and $(c+u)\Delta t$ downstream. Accelerating to supersonic speed $M > 1$, the point source travels faster than the acoustic waves in the medium. Thus the wave fronts will propagate outwards with its origin behind the current point source (point 4 in Figure 2 c)). Since the points of origin

are traveling faster than the wave fronts, a shock cone will emerge from the intersections of the waves ef.[2].

3.4 Compressible Flow

Usually when discussing fluid flow, the assumption is that changes in the fluid density due to variations of pressure, temperature and flow velocity, are negligible. When the criterion of incompressibility $M \rightarrow 0$ is observed, the majority of liquids can be analyzed and modeled (relaxed condition for modeling is discussed in Section 5) under this assumption. It is however not proper to extend the assumption into the regime of gases. When studying the compressibility of fluids, changes in density are of the same order of magnitude as the changes in pressure. And with non-trivial changes in density, one must also consider changes in the temperature that follows as the ideal gas law states. Treating incompressible flows, one needs to solve for velocity using the continuity equation

$$\frac{\partial \rho(\mathbf{x}, t)}{\partial t} + \nabla \cdot (\rho(\mathbf{x}, t) \mathbf{u}(\mathbf{x}, t)) = 0, \quad (3)$$

and for pressure through the statement of momentum conservation

$$\begin{aligned} \frac{d}{dt} \int_{V^*(t)} \rho(\mathbf{x}, t) \mathbf{u}(\mathbf{x}, t) dV + \int_{A^*(t)} \rho(\mathbf{x}, t) \mathbf{u}(\mathbf{x}, t) (\mathbf{u}(\mathbf{x}, t) - \mathbf{b}) \cdot \mathbf{n} dA \\ = \int_{V^*(t)} \rho(\mathbf{x}, t) \mathbf{g} dV + \int_{A^*(t)} \mathbf{f}(\mathbf{n}, \mathbf{x}, t) dA. \end{aligned} \quad (4)$$

For compressible flow two additional principal variables are introduced; Temperature and density. Temperature is expressed by the energy equation


$$\rho \frac{De}{Dt} = -p \frac{\partial u_m}{\partial x_m} + 2\mu \left(S_{ij} - \frac{1}{3} \frac{\partial u_m}{\partial x_m} \delta_{ij} \right)^2 + \mu_v \left(\frac{\partial u_m}{\partial x_m} \right)^2 + \frac{\partial}{\partial x_i} \left(k \frac{\partial T}{\partial x_i} \right), \quad (5)$$

and density through the equation of state, namely the Ideal gas law ef.[2]

$$pV = Nk_b T. \quad (6)$$

3.5 One-Dimensional Isentropic Pipe Flow

A cold gas thruster is essentially comprised of a large reservoir and a nozzle through which compressible gas flows. Therefore, it is meaningful to establish what a nozzle is, and find out the relationship between the pressure, density and velocity of the flow, and the cross-sectional area of the nozzle. A nozzle can be generalized to a duct of smoothly varying cross-sectional area. Under this description lies also the *diffuser*. These two devices serve the purpose of changing the flow velocity through its changing duct area. One must distinguish between three types of flow under which the nozzle and diffuser operate: (1)



Images/sonicspeed-eps-converted-to.pdf

Figure 2: *Point source traveling at three different speeds: a) stationary, b) subsonic, and c) supersonic. It is useful to represent the speed of sound in the medium as acoustic wave fronts, depicted as circles in the figure. The separation of each subsequent acoustic wave helps to visualize the relationship between the speed of sound, the speed of the point source and the angle of the shock cone α , and how it arises.*

subsonic, (2) supersonic and (3) a combination of (1) and (2). Figure 3 shows the most common configurations of a duct of smoothly varying area. To distinguish between the two devices, remember that a nozzle increases flow velocity and decreases pressure, density and temperature, while a diffuser decreases the flow velocity and increases pressure, density and pressure. Depending on whether the flow is subsonic or supersonic, the devices are designed with either a decreasing or increasing duct area cf. [3].

For the sake of simplifying the analysis, we restrict ourselves to one space dimension. Consider a control volume in a duct, seen in Figure 4. The one dimensional integrated form of the energy equation (10) becomes in this context

$$h_i + \frac{V_i^2}{2} = h_e + \frac{V_e^2}{2} \Leftrightarrow h + \frac{V^2}{2} = \text{const}, \quad (7)$$

where h is the enthalpy of the gas and V its velocity. The subscripts in Figure 4 refer to the inlet i and the exit e of the control volume. Differentiating equation (7) yields

$$dh + \frac{d(V^2)}{2} = 0. \quad (8)$$

Under the assumption that the flow is isentropic (frictionless and adiabatic) the first and second law of thermodynamics states that $dh = dp/\rho$. Inserting this into (8) we obtain

$$\frac{dp}{\rho} + \frac{d(V^2)}{2} = 0. \quad (9)$$

Leaving that aside for now, we focus on a narrower control volume, where the inlet and outlet is separated by dx and the corresponding cross-sectional area differs by dA . This is referred to as a differential control volume and can be seen in Figure 5. The one dimensional continuity equation in integrated form is

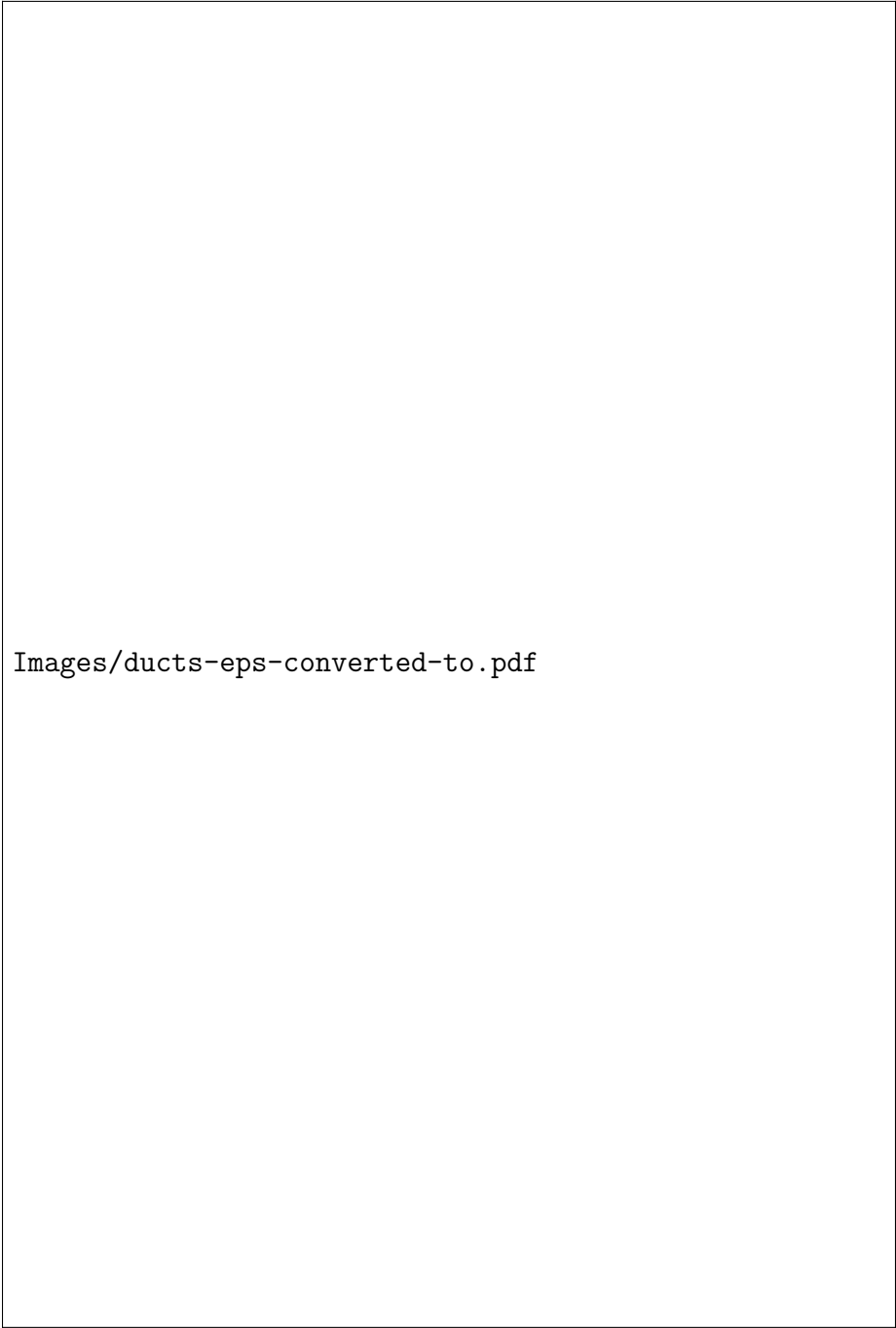
$$\rho V A = \text{const}. \quad (10)$$

Taking the logarithm and differentiating (10) yields

$$\frac{d\rho}{\rho} + \frac{dV}{V} + \frac{dA}{A} = 0 \quad (11)$$

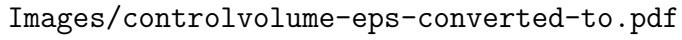
and by substituting (9) into (11) we now have

$$\frac{dA}{A} = \frac{dp}{\rho} \left(\frac{1}{V^2} - \frac{d\rho}{dp} \right). \quad (12)$$



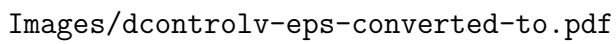
Images/ducts-eps-converted-to.pdf

Figure 3: *Subsonic, transsonic and supersonic flow through nozzles and diffusers. a) Subsonic nozzle b) supersonic nozzle c) subsonic diffuser d) supersonic diffuser e) a combination of a) and b) called a Converging-Diverging nozzle where subsonic, transsonic and supersonic flows are present.*



Images/controlvolume-eps-converted-to.pdf

Figure 4: *Control volume of a duct with varying cross sectional area. No influx of heat is present.*



Images/dcontrolv-eps-converted-to.pdf

Figure 5: *Differential control volume of width dx . No influx of heat is present.*

As seen in Figure 3, the primitive design of nozzles depends on what the mach number $M = V/c$ of the gas is throughout the duct. The speed of sound is defined as $c = \sqrt{dp/d\rho}$. Expressing (12) in terms of the mach number would therefore be helpful and looks as follows

$$\frac{dV}{V} = \frac{1}{M^2 - 1} \frac{dA}{A}, \quad (13)$$

from which the following conclusions can be made about the converging diverging nozzle (seen in the bottom of Figure 3) cf. [2, 3].

1. For a subsonic flow $M < 1$ an decrease in area leads to an increase in flow speed.
2. For a supersonic flow, a increase in area leads to an increase in flow speed.
3. Sonic speed is reached where the cross sectional area of the nozzle is minimal. This region is called the throat, and can be seen Figure 3 e).

3.6 Thrust Efficiency and Shocks

If the nozzle is not sized appropriately for the ambient pressure it operates in, it fails to deliver maximal thrust and thus efficiency is decreased. The optimal plume shape occurs when exit pressure equals ambient pressure, seen in Figure 6 b), where the plume boundary neither contracts nor expands after exiting the nozzle. If the flow in the thruster is under-expanded, as seen in Figure 6 c), means the exit pressure is higher than ambient pressure (pressure at low earth orbit, for example) and will continue expanding after exiting the thruster, thus lowering the thrust efficiency. If the ambient pressure is instead higher than the exit pressure (first stage rocket in atmospheric pressure for example), the flow is over-expanded, shown in Figure 6 a). As an effect of over and under expanded flow, discontinuities arise in the exhaust plume in the form of oblique shocks, mach discs, compression and expansion fans which in an interplay creates shock diamonds. While these shock waves may be signs of a poorly engineered nozzle, one must consider whether they are formed under the operating environment they are designed for or not. The testing of rockets usually happens under atmospheric pressure since testing in low earth orbit or in a very large vacuum chamber would be very expensive. The initial stages of a first stage rockets is under atmospheric pressure, which might not be where max efficiency is needed to be reached, so inevitably shocks appear at some point during launch. Cold gas MEMS thrusters, on the other hand, are small enough to be tested in low pressure chambers. Furthermore cold gas thrusters pose no risk of damaging the test chamber since the propellant doesn't undergo any chemical reaction which generates heat.

3.7 Sutherlands Law

Supersonic flows usually have highly varying temperature, which will affect the viscosity of the flow. Sutherlands law is an approximation of how the viscosity of a fluid depends

Images/flowchar-eps-converted-to.pdf

Figure 6: a) $P_{amb} > P_{exit}$: An over-expanded flow is "pinched" by the ambient pressure and generates shock waves starting at the separation layer, reducing efficiency. b) $P_{amb} = P_{exit}$: Thruster operating at optimal efficiency. Plume boundary is column-shaped and flow is parallel. c) $P_{amb} < P_{exit}$: An under-expanded flow continues to expand beyond the nozzle, reducing efficiency.

on the temperature. COMSOL has the option to use Sutherlands law, written as

$$\frac{\mu}{\mu_0} = \left(\frac{T}{T_0} \right)^{\frac{3}{2}} \frac{T_0 + S_\mu}{T + S_\mu}. \quad (14)$$

Sutherlands constant S_μ [K] is an effective temperature and depends on the material properties of the fluid. The constant for the most common gases and fluids can be found tabulated. If not, the constant S_μ can be computed as follows. Using the The National Institute of Standardized Technology (NIST) database, found in [4], pick two viscosities μ_0 and μ at two different temperatures T_0 and T (within the operating range of the application), correspondingly. Then solve for S_μ by using

$$S_\mu = \frac{\frac{\mu}{\mu_0} \left(\frac{T_0}{T} \right)^{\frac{3}{2}} - T_0}{1 - \frac{\mu}{\mu_0} \left(\frac{T_0}{T} \right)^{\frac{3}{2}}}. \quad (15)$$

To verify this model, plot several datapoints from the NIST data set along with the tailored Sutherland approximation. If (14) doesn't seem to follow the data points, one could change S_μ such that it does. It is not as rigorous as solving for the variable, so proceed with caution ef. [5].

4 Numerical Methods and Solvers

Having analyzed the flow inside the nozzle, we now turn our attention towards how COMSOL actually solves the complex problem of simulating compressible flow in the high mach number flow module of COMSOL. The governing equations are the non-isothermal compressible Navier Stokes equations, the Fourier heat equation and the Boltzman equation for the ambient radiation boundary conditions, which has the form

$$\rho(\mathbf{u} \cdot \nabla)\mathbf{u} = \nabla \cdot [-p\mathbf{I} + \mathbf{K}] + \mathbf{F} \quad (16a)$$

$$\nabla \cdot (\rho\mathbf{u}) = 0 \quad (16b)$$

$$\mathbf{K} = \mu \left(\nabla\mathbf{u} + (\nabla\mathbf{u})^T \right) - \frac{2}{3}\mu(\nabla \cdot \mathbf{u})\mathbf{I} \quad (16c)$$

$$\mathbf{Q} = \rho C_p \mathbf{u} \cdot \nabla T + \nabla \cdot \mathbf{q} \quad (16d)$$

$$\mathbf{q} = -k\nabla T \quad (16e)$$

$$-\mathbf{n}\mathbf{q} = \epsilon\sigma(T_{amb}^4 - T^4). \quad (16f)$$

The first five equations are solved in the fluid domain Ω_{fluid} , equation (16d) and (16e) are solved in the solid domain Ω_{solid} , while (16f) is applied as a boundary condition on some of the thrusters outward facing surfaces $\partial\Omega_{solid}$.

Solving this set of partial differential equations analytically is known to be near impossible. Therefore COMSOL discretizes the PDEs using the finite element method, and solves the discrete system of algebraic equations using a set of numerical methods. The prospect of FEM is extensively researched and excellent literature already covers the topic in great detail. However, COMSOL uses a broad range of numerical solution methods that might not be as familiar to the reader, and therefore the ones used in our simulations are covered here in some more detail.

4.1 GMRES

The high mach number flow (hmnf) physics module COMSOL uses a iterative solver called Generalized Minimized Residual (GMRES). The derivation of GMRES in this section is based on [6]. The goal in applied linear algebra always reduces down to solving some system of linear equations

$$A\mathbf{x} = \mathbf{b}. \quad (17)$$

GMRES belongs to the family of projection techniques which aims to extract an approximate solution in a subspace \mathcal{K} of \mathbb{R}^n where the exact solution \mathbf{x}^* to (17) exists. \mathcal{K}_m is called the search subspace of dimension m . In order to solve for the approximation generally m constraints must be imposed. One way is to impose the Petrov-Galerkin condition which constrains the residual vector $\mathbf{b} - A\mathbf{x}$ to be orthogonal to m linearly independent vectors

$\mathbf{b} - A\mathbf{x} \perp \mathcal{L}$. These vectors define the subspace of constraints \mathcal{L} . GMRES is an oblique projection method meaning that the subspaces are not the same (as opposed to orthogonal projections) $\mathcal{L} = A\mathcal{K}_m$ where A is the coefficient matrix of (17) and \mathcal{K}_m is the m -th Krylov subspace, with the first basis vector $\mathbf{v}_1 = \mathbf{r}/\mathbf{r}_0$. Methods using the Krylov subspace as search space are appropriately called Krylov subspace methods. GMRES is such a method and minimizes the residual norm over all vectors that can be expressed as

$$\mathbf{x} = \mathbf{x}_0 + V\mathbf{y}, \quad (18)$$

where \mathbf{y} is a vector of m dimensions and V consists of the orthogonal basis of \mathcal{K} and looks like

$$V_n = \begin{bmatrix} | & | & & | \\ \mathbf{r}_0 & A\mathbf{r}_0 & \dots & A^{n-1}\mathbf{r}_0 \\ | & | & & | \end{bmatrix}. \quad (19)$$

The residual norm operator is defined as

$$J(\mathbf{y}) = \|\mathbf{b} - A\mathbf{x}\|_2 = \|\mathbf{b} - A(\mathbf{x}_0 + V_m\mathbf{y})\|_2. \quad (20)$$

To construct the orthogonal basis V_n for the Krylov subspace we apply the Arnoldi Algorithm 1 from [6].

Algorithm 1: The Arnoldi algorithm

```

1 Choose a initial vector  $\mathbf{v}_1$  of norm 1:  $\mathbf{v}_1 = \mathbf{r}_0/\|\mathbf{r}_0\|$ 
2 for  $j=1,2,\dots,m$  do
3   for  $i=1,2,\dots,j$  do
4      $h_{ij} = (A\mathbf{v}_j, \mathbf{v}_i)$ 
5   end
6    $\mathbf{w}_j = A\mathbf{v}_j - \sum_{i=1}^j h_{ij}\mathbf{v}_i$ 
7    $h_{j+1,j} = \|\mathbf{w}_j\|_2$ 
8   if  $h_{j+1,j} = 0$  then
9     stop
10  end
11   $\mathbf{v}_{j+1} = \mathbf{w}_j/h_{j+1,j}$ 
12 end
```

Inspecting the Arnoldi Algorithm 1 we see the structure of the Hessenberg matrix, which is almost upper triangular. For example, if $m = 2$, then the Arnoldi method would construct the following Hessenberg matrices

$$\bar{H}_2 = \begin{bmatrix} (A\mathbf{v}_1\mathbf{v}_1) & (A\mathbf{v}_2\mathbf{v}_1) & (A\mathbf{v}_3\mathbf{v}_1) \\ \|w\|_1 & (A\mathbf{v}_2\mathbf{v}_2) & (A\mathbf{v}_3\mathbf{v}_2) \\ 0 & \|w\|_2 & (A\mathbf{v}_3\mathbf{v}_3) \end{bmatrix} \quad \bar{H}_3 = \begin{bmatrix} (A\mathbf{v}_1\mathbf{v}_1) & (A\mathbf{v}_2\mathbf{v}_1) & (A\mathbf{v}_3\mathbf{v}_1) \\ \|w\|_1 & (A\mathbf{v}_2\mathbf{v}_2) & (A\mathbf{v}_3\mathbf{v}_2) \\ 0 & \|w\|_2 & (A\mathbf{v}_3\mathbf{v}_3) \\ 0 & 0 & \|w\|_3 \end{bmatrix} \quad (21)$$

The algorithm also reveals, in support with Proposition 6.5 from [6], the following statement

$$AV_m = V_m H_m + \mathbf{w}_{m+1} \mathbf{e}_m^T = V_{m+1} \bar{H}_m. \quad (22)$$

We insert (18) into the residual equation of (20) and obtain

$$\mathbf{b} - A\mathbf{x} = \mathbf{b} - A(\mathbf{x}_0 + V_m \mathbf{y}) = \mathbf{r}_0 - AV_m \mathbf{y}. \quad (23)$$

Now we use proposition (22) and the fact that we set $\mathbf{v}_1 := \mathbf{r}_0/\beta$ in the GMRES algorithm. Equation (23) then becomes

$$\mathbf{b} - A\mathbf{x} = \beta \mathbf{v}_1 - V_{m+1} \bar{H}_m \mathbf{y} = V_{m+1} (\beta \mathbf{e}_1 - \bar{H}_m \mathbf{y}). \quad (24)$$

When applied to the residual norm operator J in (20), V_{m+1} can be omitted in (24) because its columns are orthonormal

$$J(\mathbf{y}) = \|\mathbf{b} - A(\mathbf{x}_0 + V_m \mathbf{y})\|_2 = \|\beta \mathbf{e}_1 - \bar{H}_m \mathbf{y}\|_2. \quad (25)$$

Thus the approximated solution to (17) is

$$\mathbf{x}_m = \mathbf{x}_0 + V_m \mathbf{y}_m, \quad (26)$$

where \mathbf{y}_m is the approximated minimizer of (20)

$$\mathbf{y}_m = \underset{\mathbf{y}}{\operatorname{argmin}} \|\beta \mathbf{e}_1 - \bar{H}_m \mathbf{y}\|_2. \quad (27)$$

Finally we summarize the theory into the GMRES Algorithm 2 from [6].

Algorithm 2: The basic GMRES algorithm

```
1 Compute  $\mathbf{r}_0 = \mathbf{b} - A\mathbf{x}_0$ , and  $\mathbf{v}_1 := \mathbf{r}_0 / \|\mathbf{r}_0\|_2$ 
2 Define the  $(m+1) \times m$  Hessenberg matrix  $\bar{H}_m = 0$ 
3 for  $j=1, 2, \dots, m$  do
4    $\mathbf{w}_j = A\mathbf{v}_j$  for  $i=1, 2, \dots, j$  do
5      $h_{ij} = (\mathbf{w}_j, \mathbf{v}_i)$ 
6    $\mathbf{w}_j = \mathbf{w}_j - h_{ij}\mathbf{v}_i$ 
7   end
8    $h_{j+1,j} = \|\mathbf{w}_j\|_2$  if  $h_{j+1,j} = 0$  then
9     set  $m := j$  and go to 13
10  end
11   $\mathbf{v}_{j+1} = \mathbf{w}_j / h_{j+1,j}$ 
12 end
13 Compute the minimizer  $\mathbf{y}_m$  of  $\|\beta \mathbf{e}_1 - \bar{H}_m \mathbf{y}\|$ , and  $\mathbf{x}_m = \mathbf{x}_0 + V_m \mathbf{y}_m$ 
```

4.2 The Multigrid Method

Iterative solvers such as Jacobi and SOR (Successive over-relaxation) perform well in smoothing out high frequency errors defined as the error gradient over the meshed domain. They are however not efficient in reducing the low frequency errors, and therefore have trouble converging with a reasonable rate for finer meshes ([7]). In every iteration of the main iterative solver, a preconditioner reduces the condition number of the coefficient matrix A in order to help resolve these low frequency errors that arise from ill conditioned systems. One such method is the Multigrid method, and while it can be used as a main solver, it is found to be highly effective when applied as a preconditioner. Nonetheless the algorithm will remain the same. The method performs a fixed number of multigrid cycles for each GMRES iteration. First it iterates few times on the fine grid of mesh size using a so called presmoothing (SOR or some other iterative solver). Thereafter it restricts the residual onto a coarser grid and applies the presmoothing again to approximate the coarse grid error. There are many structures to use for a multigrid method: V-cycle, W-cycle and F-cycle are the most common. For simplicity we shall consider the V-cycle, named after its hierarchy shape, seen in Figure 7 ef. [8, 9, 10].

The system of equations is restricted further onto a coarser mesh and the procedure is repeated until the bottom level is reached. At this level the mesh is so coarse that a direct solver can be used. COMSOL gives the option of using either MUMPS, PARDISO or SPOOLES ([10]). From the calculated residual, a correction term is added to the solution as a fine grid correction, after which a post-smoother (also SOR or other iterative method) iterates a few times on the linear system again. This is continued through levels of finer meshes until the original mesh size is h is reached. See Algorithm 2 from [9] for more details. It is up to the user to define how many levels the multigrid should consist of, and how many cycles the program should run for each iteration of the main solver. There are two multi-

Images/v-cycle.png

Figure 7: *One V-cycle in the multigrid method restricts the residual to increasingly coarser grids, until the bottom level is reached where a direct solver is used. Then the residual is interpolated upward in the hierarchy of increasing mesh resolution.* Image source: High-Performance Geometric Multi-Grid with GPU Acceleration. Nvidia.

grid types: Geometric and algebraic multigrid. The geometric multigrid creates and stores intermediate meshes for each level and is effective on structured meshes. For unstructured meshed, the algebraic multigrid creates the prolongation matrices P_i straight from the the system matrix A through Galerkin projection $A_i = P_i A_{i-1} P_i$. Thus no auxiliary mesh is created nor stored in the process. This is advantageous for unstructured grids representing a complicated geometry ([10]). Let the problem $P^{(i)}$ be defined by the right hand side $b^{(i)}$ and the coefficient matrix for the corresponding level $T^{(i)} \equiv T_{N_i \times N_i}$. The multigrid method will generate sequences of problems $P^{(i)}, P^{(i-1)} \dots P^{(1)}$ for each grid level i ([9]).

Algorithm 3: Multigrid V-cycle $MGV(b^{(i)}, x^{(i)})$

```

1 if  $i=1$  then
2   | compute exact solution  $x^{(1)}$  of  $P^{(1)}$                                 ▷ only one unknown
3   | return  $x^{(1)}$ 
4 else
5   |  $x^{(i)} = S(b^{(i)}, x^{(i)})$                                               ▷ improve solution
6   |  $r^{(i)} = T^{(i)} \cdot x^{(i)} - b^{(i)}$                                   ▷ compute residual
7   |  $d^{(i)} = In(MGV(4R(r^{(i)}), 0))$                                        ▷ solve recursively on coarser grids
8   |  $x^{(i)} = x^{(i)} - d^{(i)}$                                               ▷ correct the fine grid solution
9   |  $x^{(i)} = S(b^{(i)}, x^{(i)})$                                               ▷ improve solution
10  | return  $x^{(i)}$ 
11 end

```

Put into words, Algorithm 3 does the following:

1-3. If the problem only consists of $i = 1$ equations, then compute the exact solution. The

user can manually set the threshold for i , and use a direct solver such as PARDISO or MUMPS.

4. Else ..
5. Iterate on $P^{(i)}$ using some iterative solver $S(b^{(i)}, x^{(i)})$ (SOR, for example). This will remove errors of high frequency. At this stage the operator is called a pre-smoother.
6. Calculate the residual with the coefficient matrix $T^{(i)}$
7. (a) Calculate and map the residual to a coarser grid using the restriction operator. The restriction operator $R(b^{(i)}) = b^{(i-1)}$ maps the right hand side from problem $P^{(i)}$ to $P^{(i-1)}$.
- (b) Recursively call $MGV(4 * R(r^{(i)}), x^{(i)})$, until a user defined level is reached. Then use the interpolation operator $In(b^{(i)}, x^{(i)})$ to map the correction term back up to the finer grid.
8. Add the fine grid correction term to the solution $x^{(i)} = x^{(i)} - d^{(i)}$.
9. Iterate on $P^{(i)}$ once more using some iterative solver $S(b^{(i)}, x^{(i)})$. In this context it is referred to as a post-smoother.
10. return approximate solution $x^{(i)}$

5 Simulation Setup

5.1 COMSOL Multiphysics

COMSOL Multiphysics is a commercially available finite element analysis software for complex coupled physics problems with a wide range of numerical solvers. The simulations are computed on a *11th Gen Intel(R) Core(TM) i5-11500 @ 2.70GHz* CPU with 32.0 GB of RAM. Computations are also conducted on a laptop with *1.3GHz Intel Core i5-4250U* CPU with 8.0 GB of RAM. The University server is also used to run simulations remotely, if needed. The Siegbahn server has a *Intel(R) Xeon(R) E5520 @ 2.27GHz* CPU with 74 GB of RAM.

5.2 Thruster Model

Geometry

Since the design of the GomSpace thruster is confidential, an approximate description of the geometry is given, along with target values for the pressure temperature and mass flow at certain places in the thruster. Thus the design for the thruster, seen in in Figure 8 only resembles the actual device, but are similar enough that the simulations still gives useful insights. The thruster is made out of silicon with a length of 20mm, width 10mm and thickness 0.35mm. The silicon has a high pressure chamber that is 0.15mm thick, where

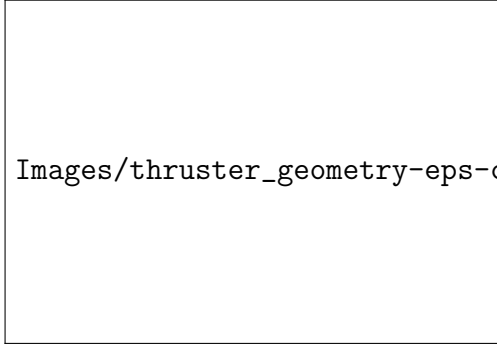


Figure 8: Design of the thruster model. The rectangular shape on top of the chip is a heating element.

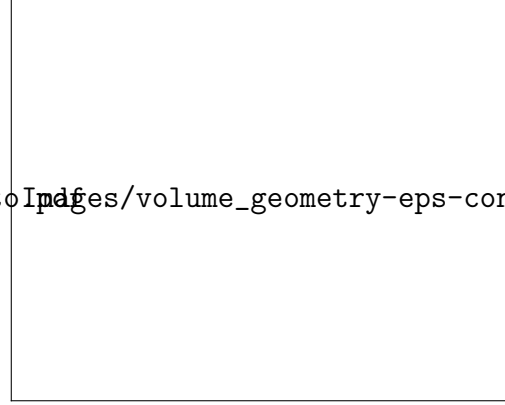


Figure 9: Design of the exhaust plume model. The volume has the dimensions $35 \times 35 \times 70\text{mm}$.

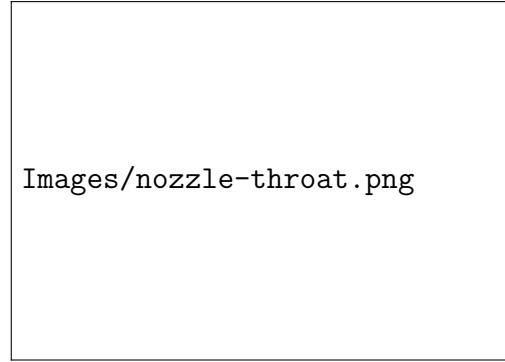
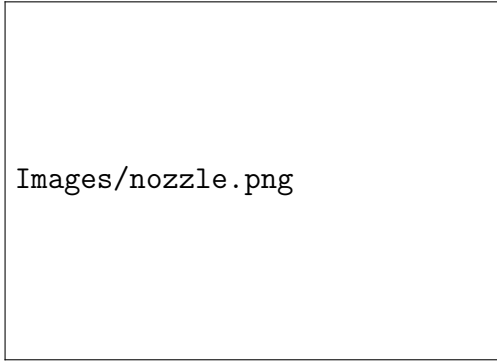


Figure 10: Parametric design of the nozzle.

butane gas operates at roughly 1 bar. The walls of the silicone chip layer has a thickness of 1mm in the xy-plane and 0.1mm along the z axis. The cavity has an circular inlet with a 1mm radius. Detailed information of the variables can be found in Table 1 and Figure 10.

Meshing

COMSOL provides a range of options for the user to define a mesh. Many different meshing methods have been tested for the models such as swept meshes, adaptive mesh refinement and box refinement. COMSOL also has the option to automatically create a mesh for the built geometry and chosen physics. For the thruster model, this automatically generated mesh seem to produce accurate results and run much smoother than the manually defined meshes. The final mesh for the thruster model is a physics based mesh for the high mach number laminar flow physics module, seen in Figure 11 and 12. The size setting is set to normal, corresponding to a total of 110434 degrees of freedom, of which 26952 are boundary elements. See Table 2 for more information about the mesh.

Table 1: *Geometric variables.*

Description	Variable	Value	Unit
Thruster Width	w_{block}	10	mm
Thruster Height	h_{block}	20	mm
Thruster depth	d_{block}	0.35	mm
Silicon thickness	d_{Si}	0.1	mm
Inlet radius	$r_i n$	1	mm
Throat radius	R_t	0.125	mm
Converging radius	r_b	1.5	mm
Diverging radius	r_a	0.382	mm
Converging angle	α_b	45	deg
Diverging angle	α_a	22.5	deg
Inlet pressure	P_{in}	1	bar
Inlet mach number	M_{in}	0.01	1
Inlet temperature	T_{in}	295	deg C



Figure 11: *Mesh illustration. The color gradient corresponds to the element size.*

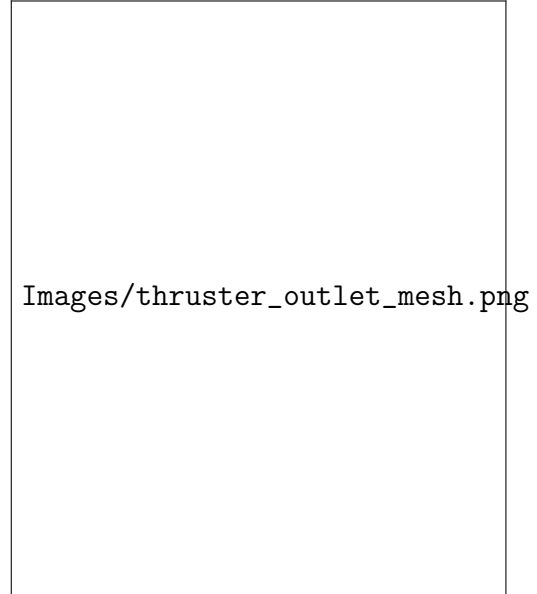


Figure 12: *Meshing size of outlet and inside nozzle. Filtering elements with logical expression $z < d_{block}/2$.*

Table 2: *Degrees of freedom and the mesh quality of the thruster model and the exhaust plume model.*

Model	Thruster	Exhaust plume
Vertex	48	48
Edge	1088	1088
Boundary	26952	18884
Total	110434	437332
Min skewness	0.02775	0.002426
Average skewness	0.529	0.6224

5.3 Exhaust Plume Model

Geometry

In the exhaust plume model seen in Figure 9 another fluid domain is connected at the nozzle exit to the fluid domain of the thruster. The volume has the dimensions $35 \times 35 \times 70\text{mm}$.

Meshing

The automatic physic based mesh can not generate a fine enough mesh where the nozzle exit and the large volume are joined. Therefore, we use a manually created mesh inspired from the physics based mesh. It is made with free tetrahedral and the geometry is split into four different domains, each with different element size settings. The size function also allows us to specify the element size for the given boundary or domain. This allows us to have a finer mesh at the surface connecting the nozzle exit and the larger volume, seen in Figure 14. The larger fluid domain has a relatively coarse mesh, too coarse to see anything meaningful in the plume. However since we expect the plume to develop along the y-axis in the middle of the volume, refining the mesh in that region is advantageous. To refine the mesh in the center of the volume along the y-axis we apply a box refinement. The box refinement enables us to define bounds for each axis and performs a regular refinement in that domain, as seen in Figure 13. We also use corner refinement to decrease the element size at sharp edges. Boundary layers are added on all the boundaries inside the thruster. This setting produces rectangular elements along the boundaries and are useful when resolving thin layer structures with no-slip conditions. Details for the meshes of the thruster model and the exhaust plume model can be found in Table 2.

5.4 Materials

COMSOL has an extensive materials library containing the properties that would be needed to define the physics taking place. Although many materials exist in the library, butane gas does not. For simulating high mach number flow (hmnf) this is not a problem. The hmnf module either treats the gas as ideal or approximates the viscosity with Sutherland's

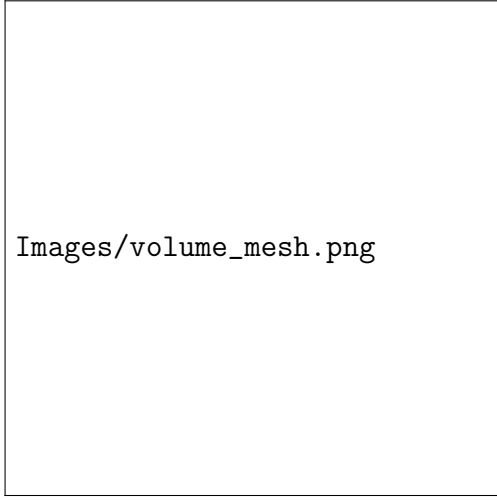


Figure 13: *Mesh size illustration of volume model. Filtering elements with logical expression $z < d - \text{block}/2$ and $x < w - \text{block}/2$.*



Figure 14: *Meshing size of nozzle exit surface that is in contact with the larger volume.*

Table 3: *Material properties for ideal butane gas.*

Property	Value	Unit
Thermal conductivity	0.017	$W/(m \cdot K)$
Specific gas constant R	143	$J/(kg \cdot K)$
Ratio of specific heat	1.096	1
Dynamic Viscosity	$7.9 \cdot 10^{-6}$	$Pa \cdot s$

law. So instead of creating a new material in the library, we define the properties of butane in the fluid flow sub-branch of the hmnf module. The material properties of butane can be seen in Table 3.

When applying surface-to-ambient radiation boundary conditions, COMSOL asks for emissivity, since it is not provided in the materials library for the materials used in this project (silicon, titanium, steel). The emissivity depends on temperature and the contact area of the material, so it is rather difficult to evaluate. Emissivity estimates of the three different materials can be seen in Table 4. These values are found in papers [11, 12].

Table 4: *Material properties for solids.*

Material	Emissivity
Silicon	0.6
Steel(AiSi4340)	0.074
Titanium	0.1

5.5 Boundary Conditions

A key part in the simulation of the chosen physics is to define the correct boundary conditions. Figures 15 and 16 display an overview of the geometry and where each boundary condition is applied.

Figure 15 displays where boundary conditions are imposed in the thruster model, and Table 5 lists what they are. At inlet (1) inflow in the normal direction is specified. The flow is specified as characteristic which means that the current flow situation is analyzed using the inviscid flow characteristics. The pressure, velocity and temperature is also defined in the boundary conditions and can be seen in Table 1. At the outlet (2) we only specify the speed-region of the flow, which in this case is supersonic. For the heat element located at (3), the boundary facing outwards is defined as thermally insulated. The surface facing inside is a heat element radiating heat with 0.3 W. (4) The upside and downside surfaces of the chip is specified as thermally insulated. This is because in reality other materials from different components would cover these surfaces. The sides of the chip (5) are specified with surface to ambient radiation. The ambient temperature is chosen as 4°K to mimic temperatures in low earth orbit. A no-slip condition is defined for the inner walls (6) of the cavity.

Table 5: *Boundary conditions for thruster model.*

#	Geometric part	Boundary condition
1	Inlet	Characteristic flow
2	Outlet	Supersonic flow
3	Heat element	Radiating heat
4	Si body (upside, downside)	Thermally insulated
5	Si body (side walls)	Surface to ambient radiation
6	Inner walls	No-slip condition

For the exhaust plume model, the outlet is connected to a large volume. The exhaust plume model also adds new boundary conditions on all outer surfaces. In Figure 16, surfaces (1) and (2) are modeled as hybrid velocity outlets with pressures of 1 Pa and 10 Pa, respectively. Surface (3) is a no-slip wall. At (4) the same boundary conditions are applied as in the thruster model, except for the heating element, which is excluded in the exhaust plume model.

6 Results

To validate the simulation of the thruster, comparisons are made with reference values given by GomSpace. The exact values are confidential, so we compare to approximate values that roughly indicates how the thruster would perform in reality. Table 6 displays these reference values along with the results we obtain in the thruster simulation.

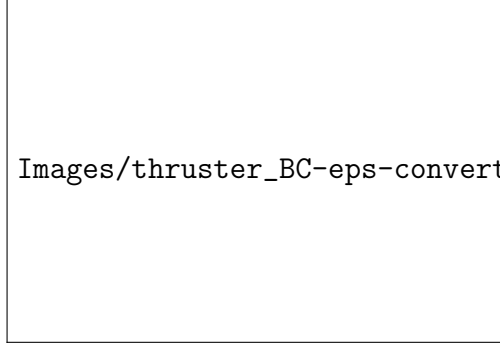


Figure 15: *Location of boundary conditions of the thruster model.*

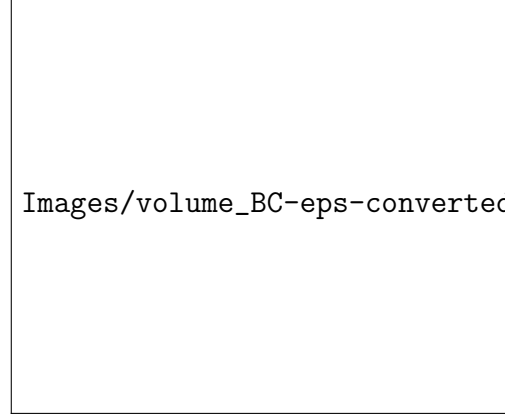


Figure 16: *Locations of boundary conditions of the exhaust plume model.*

Table 6: *Result for different materials of the thruster.*

Variables	Place	Reference	Silicon	Steel	Titanium
Velocity (m/s)	outlet	-	567.48	573.26	578.84
Max Mach number	outlet	3.5	2.92	2.92	2.92
Temperature (K)	nozzle	320	326	332.75	338.8
Temperature (K)	outlet	220	240.52	245.78	250.87
Pressure (Pa)	outlet	900	1281.9	1285.2	1288.4
Mass flow (mg/s)	nozzle	2	2.22	2.18	2.16
Mass flow (mg/s)	outlet	-	2.14	2.12	2.1

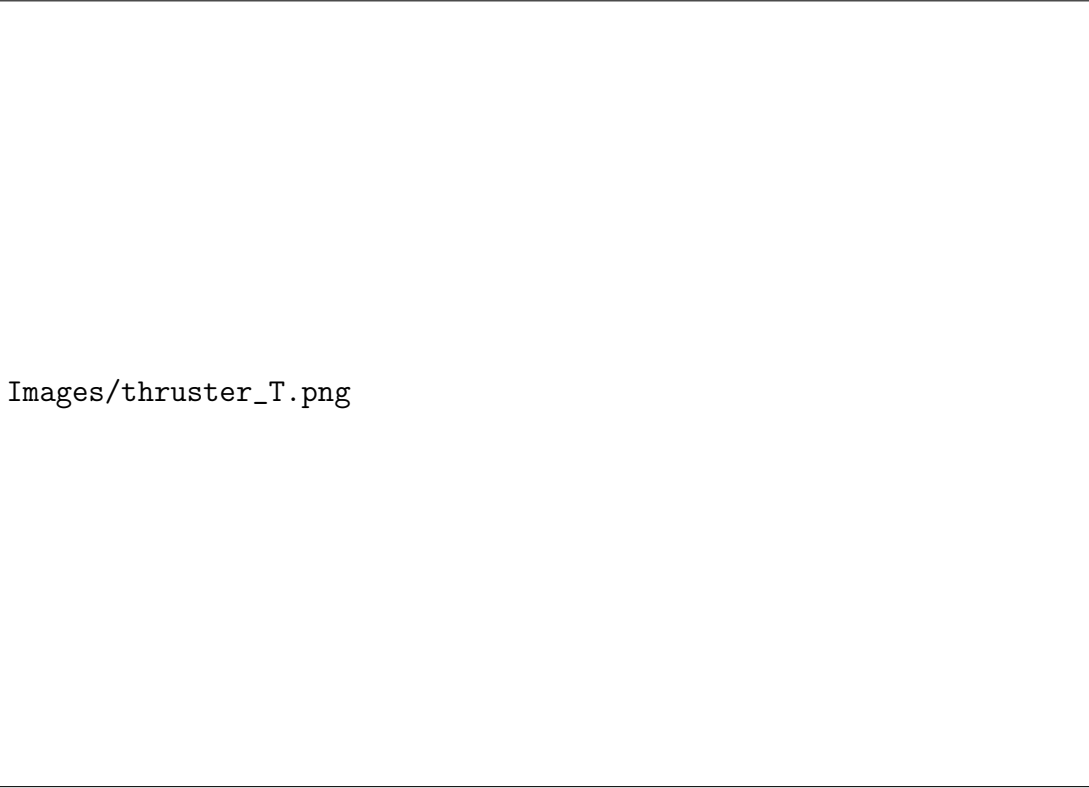
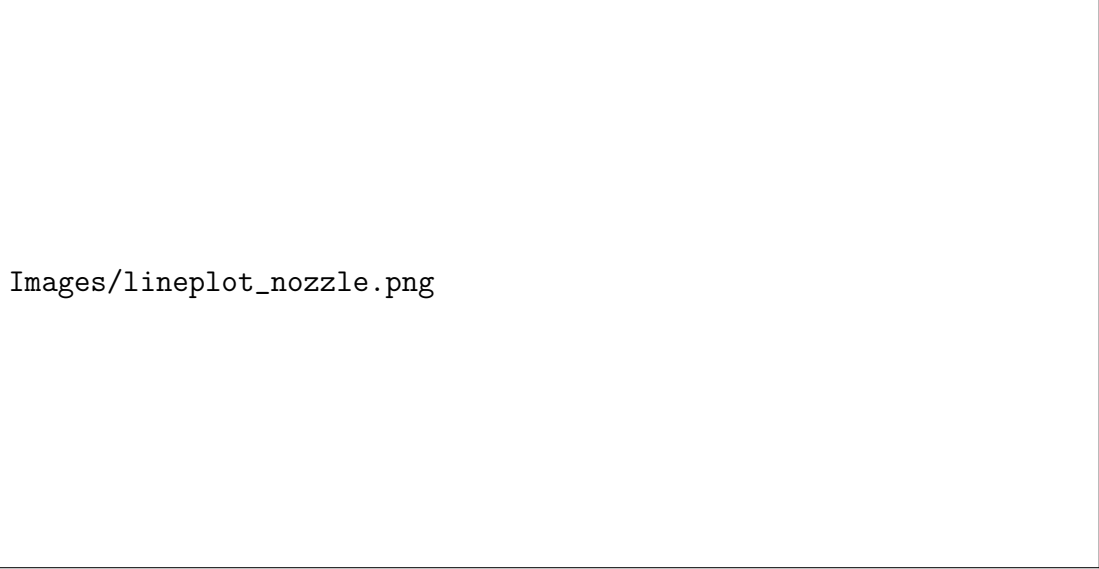


Figure 17: *Temperature of the silicon thruster and the butane gas at the cutplane $z = d_{block}/2$.*

While 3D or 2D spatial color plot provide qualitative information, quantitatively it is difficult to know the exact behavior of the flow. Therefore to more thoroughly examine the flow, we create a line plot along the center of the thruster. The lineplot for both the thruster model and the exhaust plume model can be seen in Figures (18) and (25).


6.1 Thruster Simulation

For the thruster model, the line plot in Figure 18 starts 3mm before the nozzle exit, and ends at the outlet of the thruster. For reference, Mach 1 is reached at the throat, located at arch length = 1mm. Since the three variables plotted are of different orders of magnitude, they are all normalized. At the same time it is desirable to display what the values are as well. The max values for the three variables are: $p_{max} = 1.0205 \cdot 10^5$ pa, $T_{max} = 338.45$ K $U_{max} = 567.48$ m/s. In Figure 25 the line plot starts 1mm before the throat and ends where the volume containing the exhaust plume ends.




Images/lineplot_nozzle.png

Figure 18: *Distribution of normalized variables along center of nozzle for the thruster model. The max values for the three variables are: $p_{max} = 1.0205 \cdot 10^5$ pa, $T_{max} = 338.45$ K $U_{max} = 567.48$ m/s.*



Images/thruster_U_zoom.png

Figure 19: *Velocity magnitude [m/s].*



Images/thruster_T_zoom.png

Figure 20: *Temperature [K].*



Figure 21: *Pressure* [$\log_{10}(Pa)$].



Figure 22: *Density* [$\log_{10}(kg/m^3)$].

Figure 23: *Due to large differences in pressure and density between chamber and nozzle, the base 10 logarithm has been applied, so the color gradients are not too sharp.*

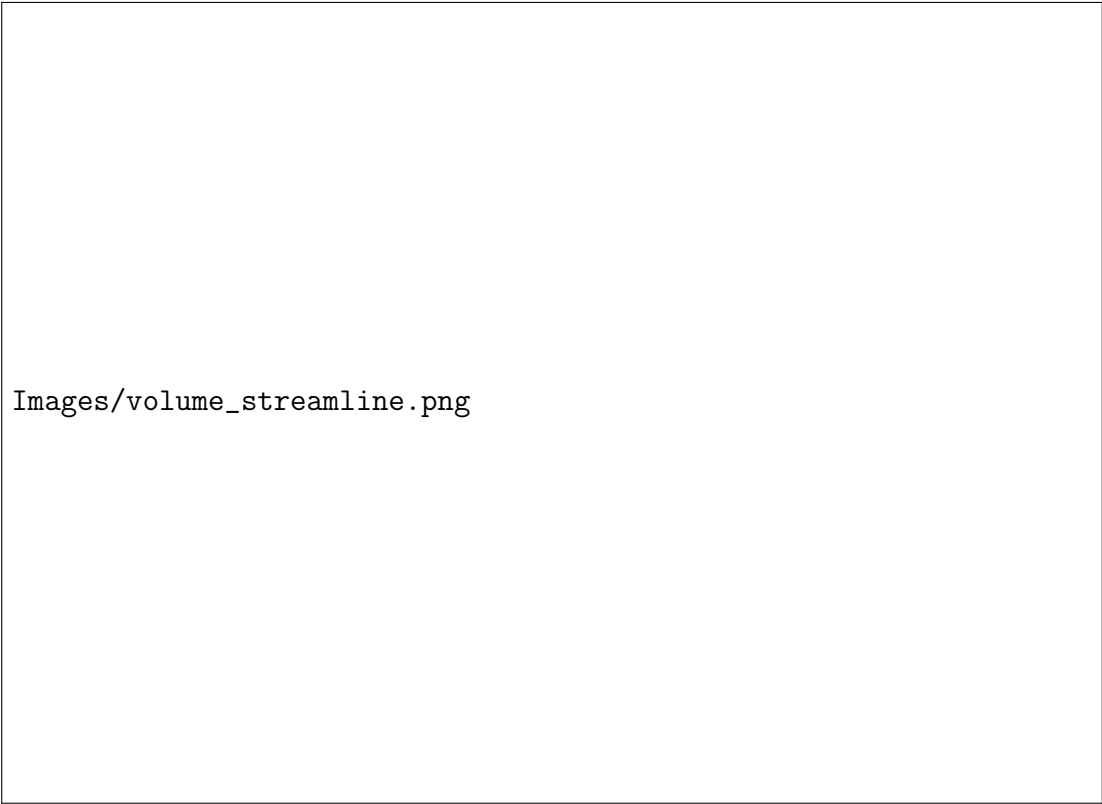
6.2 Exhaust Plume Simulation

The exhaust plume model does not have a heating element attached to the thruster as the thruster model does. The models behave similarly at the nozzle in the line plots, so meaningful insights that apply to both models can still be drawn, although the exact numeric results can't be compared. We make two modifications in the pressure and density plots in Figure 28 and 29. Firstly, we apply the base 10 logarithm to smooth out the otherwise sharp color gradient at the throat of the nozzle. Secondly, we manually set the color range to be more narrow, so that the fluctuation stand out more. What happens in the thruster is not focused on here and can instead be seen in the thruster simulation section above. Accompanying the x-y plots (located on the left in the collage above) are the line plots, seen in Figure 25. This helps to couple the 2D and 1D plots to gain better understanding of whats happening.

7 Discussion


7.1 Meshing Options

When constructing the geometry, it is easy to forget how important a well defined mesh is for the convergence of the solution. As the geometry is very thin, a mesh size of h may suffice in the x-y dimensions of the thruster, but not in the z direction where the thickness is close to h . There are many ways to overcome this, for example the size function generates



Images/volume_streamline.png

Figure 24: *A qualitative plot of how the gas is behaving in the exhaust plume. The 2D plots are projected from the center to the sides, to not obstruct the streamlines.*



Images/volume_lineplot.png

Figure 25: *Distribution of normalized variables along center of nozzle for the exhaust plume model.*

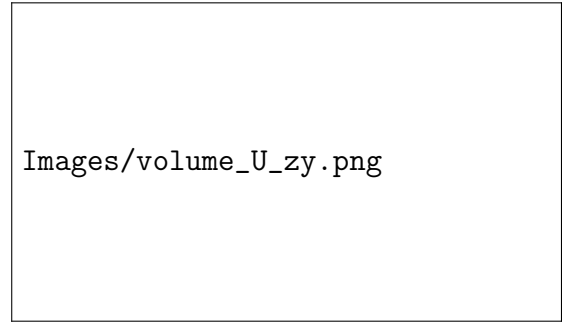
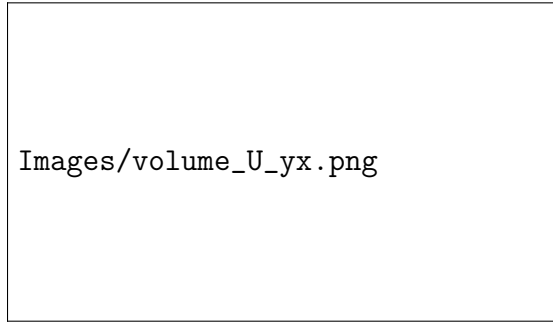


Figure 26: *Velocity magnitude of the gas flow.*

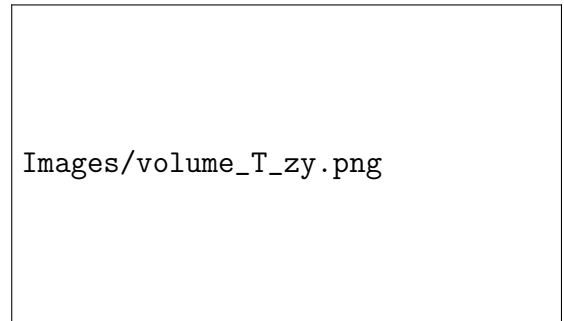
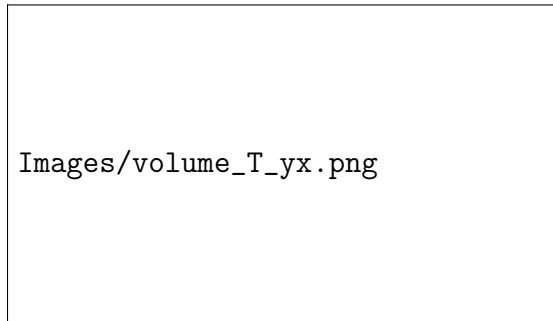


Figure 27: *Temperature of the gas flow and the thruster.*

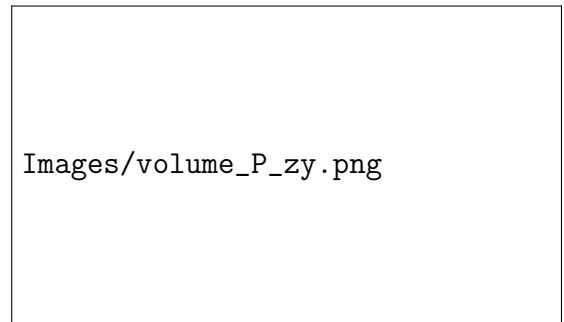
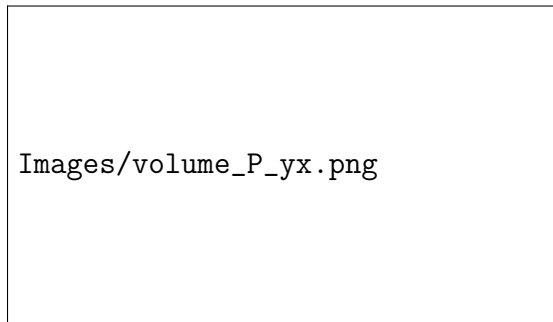


Figure 28: *\log_{10} of the gas pressure.*

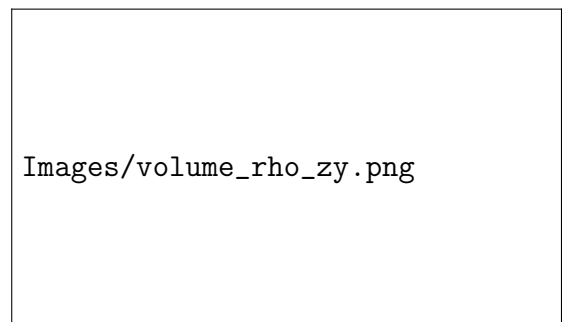
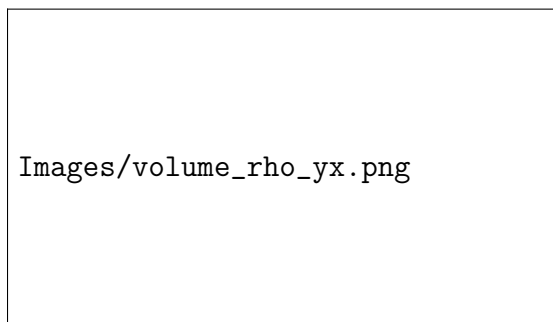


Figure 29: *\log_{10} of the gas density.*

different sized meshes on different domains and boundaries. Another maybe more suitable way to solve the problem is the swept mesh method. It projects the mesh of one surface to another to preserve some regularity in between. The caveat with this is that the so called source face and the destination face must have the same shape. In our case this works for the fluid domain, but not for the solid domain of the thruster, as one can't sweep past the cavity inside. However, the swept mesh results in a solution with a high residual, so for the thruster model we instead use a predefined physics based mesh for high mach number flow. For the exhaust plume model we define a box in which the elements would be regularly refined in the regions we deem interesting. Meshing a thin structure is also problematic when attaching a volume at the nozzle exit to model the exhaust plume. If the mesh resolution on the connecting surfaces isn't fine enough, not enough information about the flow pass through and it will look like an invisible wall is obstructing the flow.

Another approach to further increase the mesh quality to better distinguish the shockwaves is to use the error estimated mesh refinement. Compared to the box refinement we use, this method does not require the user to know the needed refinement areas. It is probable that this will produce less DOF while keeping the mesh fine in the interesting areas.

7.2 Exhaust Plume Model Results

Figure 24 illustrates the particle trajectories. The coloring of the streamlines represent the temperature. The 2D plots are offset from the center and displays the mach number of the flow. There are numerous things to observe here. First and most notable is that the plume is not axi-symmetric seen in Figures 26-29. This make sense since the nozzle is not axi-symmetric either. We further see that the plume expands a lot more in the direction of the thusters shortest sides, the z direction. This makes sense given that the height of the nozzle are fixed in the z - y plane seen in the right plot of Figure 28. This restricts the pressure from dropping until it reaches the exit. In the x - y plane view, seen in the left plot of Figure 28 we can see the characteristic "Converging-Diverging" nozzle shape. The diverging part allows for a more substantial pressure drop, meaning that it dont expand as much in the x - y plane after exiting the thruster.

In the line plot of the exhaust plume model in Figure 25, the velocity increases rapidly, and the temperature doesn't drop to what one would experience in low earth orbit pressures. One could possibly argue that the volume in the plume model is not long enough. But observe the behavior of the pressure in Figure 29, it drops to near zero in and around the plume. Remember that in the physics module of COMSOL the equation of state is the Ideal gas law. And as pressure drops, density drops, so the specific energy of the flow would looks very different compared to the temperature. This is a major flaw in modeling gas flow in a vacuum. Examining the enthalpy or energy of the flow would give a better understanding of the fluid. After all, calculating the total energy of the flow is similar to weighting the temperature and velocity by the density. The rarefied-flow module in COMSOL yields better results in this aspect, since it treats gas-vacuum interfaces. It is not clear to us whether it also includes the physics of compressible flow. Another observation is that the

pressure continues to drop after the outlet (located at the second vertical dashed line in Figure 25), which suggests that the flow is under-expanded. Under expanded flow (and over expanded, for that matter) produces shock waves that starts from the outer walls of the nozzle exit, and are directed diagonally inward and along the fluid flow. In turn they produce a mach discs. Maybe that is what we can see in 26 at $x=0.03\text{m}$, about 10mm from the nozzle exit. While this is not wanted, the effect does not seem to be that severe as no significant expansion or compression fans, oblique shocks or shock diamonds are developed downstream.

7.3 Fidelity of COMSOLs Solution

The main objective in the project is to create a COMSOL model with satisfactory accuracy and fidelity. As stated before, the setup is not entirely true to the the real device and the environment it is subject to. Furthermore than the use of not exact geomentry, thrusters don't simply float in space, thus having no interaction but black body radiation, as our model suggests. The thruster is attached to a PCB board, a gas pipe delivering high pressure butane and a pressure sensor, which all in turn have contact with the rest of the propulsion module and the cube-sat. All these components that are not present in the COMSOL model acts as heat sinks and should not be deemed trivial. One way to circumvent this is to experimentally determine the heat transfer coefficients at the area of contact for each respective component and thruster, so a heat flux boundary condition could be imposed. Furthermore, it might be of interest to take into account that all these components emits black body radiation as well.

Continuing on the topic of radiation. There is no convection or diffusion of heat taking place in a vacuum, making radiation the only means for heat transfer. Consequentially, when one side of the satellite is exposed to solar radiation, and the other faces space or earth, large thermal gradients develops. Thermal gradients will make for uneven thermal expansion of the spacecraft, which can damage components if not taken into account.

GMRES and multigrid method prove to be successful in approximating a solution that is satisfactory for the means and purposes of this study. These solvers however, have many parameters that can tailor the method for the specific problem. It is far from obvious what the best configurations are to get a solution to converge with a sufficiently small error. For iterative methods like GMRES, COMSOL uses the error estimate criterion $\rho|M^{-1}(\mathbf{b} - A\mathbf{x})| < tol \cdot |M^{-1}\mathbf{b}|$. Put into words, the preconditioned residual $M^{-1}\mathbf{r} = M^{-1}(\mathbf{b} - A\mathbf{x})$ (M is a preconditioner matrix) must be less than the tolerance tol times a factor ρ . If the equation system still is ill conditioned, then the inverse A^{-1} might be very large. This makes the error large, even though the residual might be small. Consider the error $\mathbf{e} = A^{-1}\mathbf{r}$. If $A^{-1} \approx 10^6$ and $\mathbf{r} \approx 10^{-4}$, then the error will be on the magnitude of 10^2 . The system of equations also depend on how well the geometry is discretized and what size the elements are. Our approach to refine in select regions of the plume-domain

leaves the rest of the region with very large elements.

8 Conclusions

The results shows that the material property which is the the biggest impact on the thermal gradient in the solid and gas of the thruster is not the thermal conductivity as we expected, but the surface emissivity for each material. Based on the physics this makes sense. As the thruster in the simulation is not in contact with any other components, the surface to ambient radiation which depends on the surface emissivity is the only heat sink in the model. To make the model more realistic adding heat sinks with empirically derived heat transfer coefficients is advised in future studies. The exhaust plume is underexpanded as a sharp pressure gradient is observed at the nozzle exit, meaning the efficiency is not optimal. The study is stationary, meaning we only look at the solution at thermal equilibrium. Although this does provide meaningful insights into the characteristics of the flow, a time-dependent study would be interesting for future work, given the thrusters operates in short bursts that won't reach the equilibrium.

Acknowledgements

Our project course supervisor Prof. Maya Neytecheva managed to provide us with individual licenses for our personal computers. We express our gratitude towards Professor Neytecheva and COMSOL. We also would like to thank GOMSPACE Sweden for being a good collaborative partner during the project.

References

- [1] Mary-Ann Russon, “Satellite boom attracts technology giants.” <https://www.bbc.com/news/business-55807150>. Accessed: 2022-02-01.
- [2] I. M. C. Pijush K. Kundu, *Fluid Mechanics*. Academic Press, 2002.
- [3] R. A. Granger, *Fluid Mechanics*. Dover Publications, INC, 1995.
- [4] NIST, “Thermophysical Properties of Fluid Systems.” <https://webbook.nist.gov/chemistry/fluid/>. Accessed: 2022-01-20.
- [5] COMSOL, “Sutherland’s Law.” https://doc.comsol.com/5.5/doc/com.comsol.help.cfd/cfd_ug_fluidflow_high_mach.08.27.html. Accessed: 2022-01-20.
- [6] Y. Saad, “Iterative Methods for Sparse Linear Systems,” *Notes*, vol. 3, no. 2nd Edition, pp. xviii+528, 2003.
- [7] COMSOL, “Multigrid.” https://www.cfd-online.com/Wiki/Multigrid_methods. Accessed: 2022-01-25.
- [8] COMSOL, “Multigrid.” https://doc.comsol.com/5.5/doc/com.comsol.help.comsol/comsol_ref_solver.27.158.html. Accessed: 2022-01-25.
- [9] J. W. Demmel, *Applied Numerical Linear Algebra*. Society for Industrial and Applied Mathematics, 1997.
- [10] COMSOL, “The Multigrid Algorithm.” https://doc.comsol.com/5.5/doc/com.comsol.help.comsol/comsol_ref_solver.27.124.html. Accessed: 2022-01-25.
- [11] P. O. Cervenka and L. Massa, “Applications of dimensionless variables to scaling in the infrared,” tech. rep., NAVAL SURFACE WARFARE CENTER CARDEROCK DIV SILVER SPRING MD, 1995.
- [12] M. Constancio Jr, R. X. Adhikari, O. D. Aguiar, K. Arai, A. Markowitz, M. A. Okada, and C. C. Wipf, “Silicon emissivity as a function of temperature,” *International Journal of Heat and Mass Transfer*, vol. 157, p. 119863, Aug 2020.